# HEAT TRANSFER, VELOCITY-TEMPERATURE CORRELATION, AND TURBULENT SHEAR STRESS FROM NAVIER-STOKES COMPUTATIONS OF SHOCK WAVE/TURBULENT BOUNDARY LAYER INTERACTION FLOWS

C.R. Wang, W.R. Hingst, and A.R. Porro
National Aeronautics and Space Administration
Lewis Research Center
Cleveland, Ohio 44135

## ABSTRACT

The properties of two-dimensional shock wave/turbulent boundary layer interaction flows were calculated by using a compressible turbulent Navier-Stokes numerical computational code. Interaction flows caused by oblique shock wave impingement on the turbulent boundary layer flow were considered. The oblique shock waves were induced with shock generators at angles of attack less than 10° in supersonic flows (Mach 2.5 and 6.0). The surface temperatures were kept at near-adiabatic (ratio of wall static temperature to free-stream total temperature, 0.99) and cold-wall (ratio of wall static temperature to free-stream total temperature, 0.66) conditions. The computational results were studied for the surface heat transfer, velocity-temperature correlation, and turbulent shear stress in the interaction flow fields. Comparisons of the computational results with existing measurements indicated that (1) the surface heat transfer rates and surface pressures could be correlated with Holden's relationship, (2) the mean flow streamwise velocity components and static temperatures could be correlated with Crocco's relationship if flow separation did not occur, and (3) the Baldwin-Lomax turbulence model should be modified for turbulent shear stress computations in the interaction flows.

## NOMENCLATURE

| | |
|---|---|
| $C_{cp}$ | empirical constant for turbulence modeling |
| $C_f$ | skin friction factor |
| $C_v$ | specific heat at constant volume |
| $C_{wk}$ | empirical constant for turbulence modeling |
| E,F | vectors |
| $F_{kleb}$ | Klebanoff intermittency factor |
| $F_{wake}$ | turbulence modeling factor |
| H | grid dimension (fig. 1(a)) |
| IM | grid dimension (fig. 1(b)) |

| | |
|---|---|
| $J$ | Jacobian matrix |
| $JM$ | grid dimension (fig. 1(b)) |
| $k$ | empirical constant for turbulence modeling |
| $L$ | grid dimension (fig. 1(a)) |
| $\ell$ | length scale for turbulence modeling |
| $M$ | Mach number |
| $Pr$ | laminar Prandtl number |
| $Pr_t$ | turbulent Prandtl number |
| $p$ | static pressure |
| $p_{O2}$ | pitot pressure |
| $p_{O\infty}$ | free-stream total pressure |
| $Q$ | heat transfer rate |
| $Re_{\delta O}$ | free-stream Reynolds number, $\rho_e U_e \delta_O / \mu_e$ |
| $T$ | static temperature |
| $T_{O\infty}$ | free-stream total temperature |
| $t$ | time |
| $U$ | mean flow velocity component |
| $U_\tau$ | friction velocity |
| $u'$ | turbulent fluctuation in $U$ |
| $V$ | mean flow velocity component |
| $v'$ | turbulent fluctuation in $V$ |
| $X$ | distance along streamwise direction |
| $X_C$ | location where minimum grid occurs |
| $Y$ | normal distance from wall |
| $Y_C$ | value of $Y$ at which $\varepsilon$ values from inner and outer formulas are equal |
| $\alpha$ | stretching factor |
| $\beta$ | stretching factor |

| | |
|---|---|
| $\gamma$ | recovery factor |
| $\delta_o$ | initial boundary layer thickness |
| $\varepsilon$ | eddy viscosity |
| $\eta$ | transformed coordinate in Y-direction |
| $\theta$ | angle of attack |
| $\lambda$ | stretching factor |
| $\mu$ | absolute viscosity |
| $\xi$ | transformed coordinate in X-direction |
| $\rho$ | density |
| $\tau XX, \tau XY, \tau YY$ | normal or shear stress |
| $\omega$ | magnitude of vorticity |

Subscripts:

| | |
|---|---|
| dif | difference between maximum and minimum values |
| e | far-field condition |
| max | maximum |
| min | minimum |
| o | condition at X = 0 |
| r | reference condition |
| w | surface condition |
| $\infty$ | free-stream condition |

## INTRODUCTION

Because of recent development efforts for supersonic and hypersonic flight vehicles, generic research in the flow fields of advanced propulsion systems has become an interesting topic of compressible flow studies. Shock wave/turbulent boundary layer interaction flow is an important, basic flow phenomenon within the flow fields of supersonic or hypersonic propulsion systems. The variations of velocity components, surface pressures, and skin friction factors within the interaction flow fields have been studied, and a review of the existing literature is reported by Delery, Marvin, and Reshotko (ref. 1). Under severe operational conditions, surface heat transfer becomes an important element in the design of an advanced propulsion system. From an effort to study the surface heat transfer beneath shock wave/turbulent boundary layer interaction flows, the present authors describe in this paper some preliminary results of their computational analyses of the flow properties in

several two-dimensional shock wave/turbulent boundary layer interaction flows. The flow properties were computed by using the Navier-Stokes numerical code developed by Shang, Hankey, and Law (ref. 2), and the computational results were compared with the experimental measurements of Hingst and Porro (W.R. Hingst and A.R. Porro, NASA Lewis Research Center, Cleveland, Ohio, 1989, personal communication), Alzner and Zakkay (ref. 3), and Zakkay and Wang (ref. 4).

First, the shock wave/turbulent boundary layer interaction flows in a Mach 2.5 free stream were studied. Hingst and Porro performed experiments with this type of interaction flow field. They used a shock generator plate at an angle of attack with a Mach 2.5 free stream to produce oblique shock. The interaction of the oblique shock with the naturally occurring boundary layer on the tunnel wall defined the experimental configurations. Tests were conducted to measure the surface static pressure, surface dynamic pressure, and surface heat transfer with near-adiabatic and heated surfaces. The experimental results with the shock generator at 4° and 8° angles of attack were used to verify the present computations.

Second, the shock wave/turbulent boundary layer interactions induced by inserting axisymmetric wedges (wedge angles 4° and 10°) in a Mach 6 free stream were studied. Alzner and Zakkay (ref. 3) and Zakkay and Wang (ref. 4) performed experiments in these flow fields. They measured the surface heat transfer rates, static pressures, and pitot pressures. The turbulent boundary layer developed along a cylindrical center body surface. The ratio between the surface temperature and the total temperature was 0.66. This represented a cold wall condition. These experimental results were used to verify the present computations. This study of Mach 6 interaction flow is important since, in the existing literature, Navier-Stokes computations are limited mostly to Mach 3 cases with adiabatic wall conditions.

Since Shang's Navier-Stokes equation computational code used the Baldwin-Lomax turbulence model (ref. 5), we investigated the capability of this turbulence model in the Navier-Stokes computational code to predict the turbulent shear stresses in an interaction flow. The Reynolds shear stress in a Mach 2.9 interaction flow was also computed. Rose and Johnson (ref. 6) measured the turbulence shear stresses in Mach 2.9 interaction flow. Their turbulence measurements were compared with our computations of Reynolds stress.

The present computational results of the streamwise mean flow velocity components and static temperatures were correlated and compared with Crocco's relationship (ref. 7). The surface pressures and heat transfer rates from the computations were also correlated and compared with Holden's relationship (ref. 8). With these comparisons, the applications of Crocco's and Holden's relationships to estimate the surface heat transfer rates and temperature variations in shock wave/turbulent boundary layer interaction flow are discussed. The preliminary Reynolds stress computations were studied to determine the applicability of Baldwin-Lomax turbulence modeling in interaction flows.

## COMPUTATIONAL METHODS

A time-dependent explicit numerical computational code was used to solve the compressible turbulent Navier-Stokes equations and the energy equation for steady-state interaction flow properties. This code was developed (ref. 2) by

using MacCormack's finite difference computational scheme (ref. 9). In this code, the physical domain (X,Y) was transformed into a computational domain ($\xi$,$\eta$) with a uniform computational grid along both $\xi$ and $\eta$ axes. Details of the mathematical manipulations in the coordinate transformations related to the Navier-Stokes equations are given in the text book by Anderson, Tannehill, and Pletcher (ref. 10). However, the conservation equations, coordinate transformations, turbulence modeling, initial and boundary conditions, and numerical scheme used in this study are described briefly in the following paragraphs.

**Conservation Equations**

The following two-dimensional compressible turbulent Navier-Stokes equations and total energy equation

$$\frac{\partial U}{\partial t} + \frac{\partial E}{\partial X} + \frac{\partial F}{\partial Y} = 0 \tag{1}$$

with

$$U = \begin{bmatrix} \rho \\ \rho U \\ \rho V \\ E_t \end{bmatrix}$$

$$E = \begin{bmatrix} \rho U \\ \rho U^2 + p - \tau_{XX} \\ \rho UV - \tau_{XY} \\ (E_t + p)U - U\tau_{XX} - V\tau_{XY} + Q_X \end{bmatrix}$$

$$F = \begin{bmatrix} \rho V \\ \rho UV - \tau_{XY} \\ \rho V^2 + p - \tau_{YY} \\ (E_t + p)V - U\tau_{XY} - V\tau_{YY} + Q_Y \end{bmatrix}$$

where

$$E_t = \rho\left(C_v T + \frac{U^2 + V^2}{2}\right)$$

$$\tau_{XX} = \frac{4}{3}(\mu + \varepsilon)\frac{\partial U}{\partial X} - \frac{2}{3}(\mu + \varepsilon)\frac{\partial V}{\partial Y}$$

$$\tau_{YY} = \frac{4}{3}(\mu + \varepsilon)\frac{\partial V}{\partial Y} - \frac{2}{3}(\mu + \varepsilon)\frac{\partial U}{\partial X}$$

$$\tau_{XY} = (\mu + \varepsilon)\left(\frac{\partial V}{\partial X} + \frac{\partial U}{\partial Y}\right)$$

$$Q_X = \frac{C_v \mu}{Pr}\frac{\partial T}{\partial X} + \frac{C_v \varepsilon}{Pr_t}\frac{\partial T}{\partial X}$$

$$Q_Y = \frac{C_v \mu}{Pr}\frac{\partial T}{\partial Y} + \frac{C_v \varepsilon}{Pr_t}\frac{\partial T}{\partial Y}$$

were used to describe the variations of flow properties within two-dimensional interaction flow. In these equations, the turbulence contributions to the momentum and energy transports were related to the gradients of the mean velocity components and the mean static temperature by using the concepts of turbulent eddy viscosity and the Reynolds analogy. A laminar Prandtl number $Pr = 0.73$ and a turbulent Prandtl number $Pr_t = 0.90$ were chosen. These Navier-Stokes equations were written in a two-dimensional orthogonal X-Y coordinate system. Thus, the effect of the center body radius on the axisymmetric interaction flows (refs. 3 and 4) was not considered.

## Coordinate Transformations

Figure 1 presents the general concept of the transformations between the physical and the computational domains. The transformations were required to concentrate the computational mesh points within the region where large gradients in the flow properties would occur in the physical domain. Similar

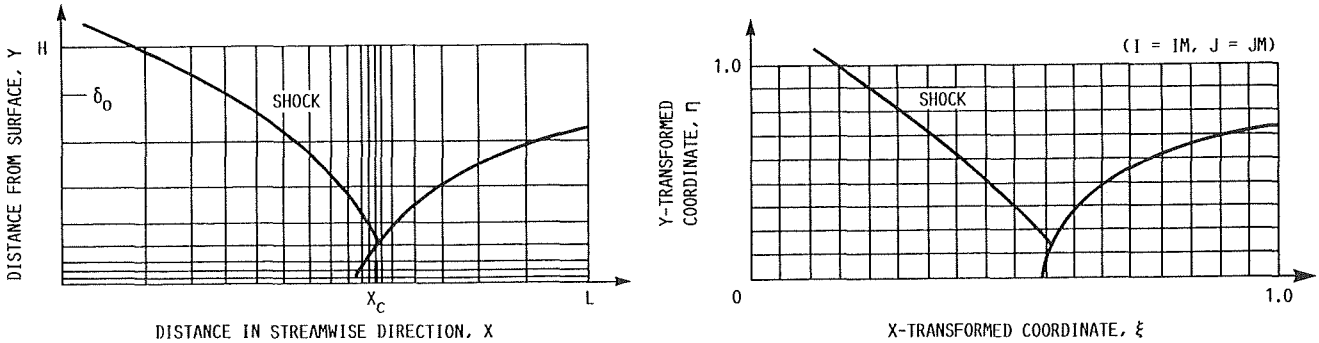


FIGURE 1. - COMPUTATIONAL GRIDS IN PHYSICAL AND COMPUTATIONAL DOMAINS.

coordinate transformations are described in reference 10, and the following transformations were used in this study:

$$\xi = \alpha + \frac{\sinh^{-1}\left[(X/X_c - 1)\sinh(\lambda\alpha)\right]}{\lambda} \tag{2}$$

and

$$\eta = 1 - \frac{\ell n\{[\beta + 1 - (Y/H)]/[\beta - 1 + (Y/H)]\}}{\ell n[(\beta + 1)/(\beta - 1)]} \tag{3}$$

where

$$\alpha = \frac{L}{2\lambda} \ell n \left[ \frac{1 + (e^{\lambda} - 1)(X_c/L)}{1 + (e^{-\lambda} - 1)(X_c/L)} \right]$$

with

$$0 \leq \lambda \leq \infty \quad \text{and} \quad 1 \leq \beta \leq \infty$$

Different sizes of the physical domain, the computational grid dimensions IM and JM, and the numerical values for $\lambda$ and $\beta$ were chosen for different flow configurations. Together with the computational results, these parameters are presented for each flow field in the latter part of this paper.

**Turbulence Modeling**

The algebraic turbulence model proposed by Baldwin and Lomax (ref. 5) was used here. It is a two-layer algebraic eddy viscosity model in which the eddy viscosity $\varepsilon$ is given by

$$\varepsilon = \begin{cases} \varepsilon_{inner} & Y < Y_c \\ \varepsilon_{outer} & Y \geq Y_c \end{cases}$$

where $Y$ is the normal distance from the wall and $Y_c$ is the value of $Y$ at which $\varepsilon$ values from the inner and outer formulas are equal. For a two-dimensional mean flow, the eddy viscosity model can be written as follows:

In the inner layer,

$$\varepsilon = \rho \ell^2 |\omega|$$

where

$$\ell = kY\left[1 - \exp\left(-\frac{Y^+}{A^+}\right)\right]$$

$|\omega|$ is the magnitude of the vorticity

$$|\omega| = \sqrt{\left(\frac{\partial U}{\partial Y} - \frac{\partial V}{\partial X}\right)^2}$$

and

$$Y^+ = \frac{\rho_w U_\tau Y}{\mu_w}$$

In the outer layer,

$$\varepsilon_{outer} = kC_{cp}\rho F_{wake} F_{kleb}$$

where

$$F_{wake} = \text{the smaller of} \begin{cases} Y_{max}F_{max} \\ \text{or} \\ \dfrac{C_{wk}Y_{max}U_{dif}^2}{F_{max}} \end{cases}$$

and

$$F(Y) = Y|\omega|\left[1 - \exp\left(-\frac{Y^+}{A^+}\right)\right]$$

The quantity $F_{max}$ is the maximum value of $F$ that occurs in a profile and $Y_{max}$ is the value of $Y$ at which it occurs. The function $F_{kleb}(Y)$ is the Klebanoff intermittency factor given by

$$F_{kleb} = \left[1 + 5.5\left(\frac{C_{kleb}Y}{Y_{max}}\right)^6\right]^{-1}$$

The quantity $U_{dif}$ is the difference between the maximum and minimum total velocities in the profile:

$$U_{dif} = \left(\sqrt{U^2 + V^2}\right)_{max} - \left(\sqrt{U^2 + V^2}\right)_{min}$$

The second term in $U_{dif}$ is set to be zero.

Baldwin and Lomax determined a set of values for the empirical constants appearing in the above relationships. These values are $A^+ = 26$, $C_{cp} = 1.6$, $C_{kleb} = 0.3$, $C_{wk} = 0.24$, $k = 0.4$, and $\kappa = 0.0168$. However, a different value for $C_{cp} = 2.0$ was used in the present computations.

**Numerical Computational Scheme**

The governing equations were transformed from the physical domain to the computational domain. The chain rule of partial differentiation was used to rewrite equation (1) as

$$\frac{\partial U_1}{\partial t} + \frac{\partial E_1}{\partial \xi} + \frac{\partial F_1}{\partial \eta} = 0 \qquad (4)$$

where

$$U_1 = \frac{U}{J}$$

$$E_1 = \frac{E\xi_X + F\xi_Y}{J}$$

$$F_1 = \frac{E\eta_X + F\eta_Y}{J}$$

and $J$ is the Jacobian matrix of the transformation.

The vectors $E_1$ and $F_1$ contain partial derivatives in the viscous and heat transfer terms. These partial derivative terms were also transformed by using equations (2) and (3).

An explicit MacCormack predictor and corrector time iteration with a fourth-order smoothing numerical scheme was used to solve the Navier-Stokes equations for the flow properties within the interaction flow region. Forward finite differencing and backward finite differencing were chosen respectively for the differentiations in the predictor and the corrector steps. The stability factors for CFL and the smoothing terms in the X and Y directions were 0.9, 0.4, and 0.4, respectively, in all of the computations.

The existing Navier-Stokes equation solver (ref. 2) used a time-dependent explicit computational scheme. The initial flow properties and their conditions around the boundary of the physical domain were required to start the computations. With one exception, which will be described later, the following general principles specified the initial and boundary conditions.

**Initial Conditions**

The properties of a fully developed flat plate turbulent boundary layer flow were used in the initial conditions. These properties were calculated by using the Navier-Stokes equation solver. For this purpose, the initial mean velocity profiles

$$\frac{U}{U_e} = \left(\frac{Y}{\delta_o}\right)^{1/7} \quad \text{and} \quad V = 0$$

were assumed. The local temperature was related to the mean velocity component $U$ by Crocco's relationship,

$$\frac{T}{T_e} = \frac{T_w}{T_e} + \left(1 + 0.2\gamma\, M_e^2 - \frac{T_w}{T_e}\right)\left(\frac{U}{U_e}\right) - 0.2\gamma\, M_e^2\left(\frac{U}{U_e}\right)^2 \qquad (5)$$

with the recovery factor $\gamma = 0.9$.

**Boundary Conditions**

For the initial boundary layer flow computation, the far-field boundary conditions were described by the free-stream conditions. They are $\rho = \rho_e$, $U = U_e$, $V = 0$, and $T = T_e$.

The following conditions,

$$U = 0 \qquad V = 0 \qquad T = T_w \quad \text{and} \quad \frac{\partial p}{\partial Y} = 0 \tag{6}$$

were specified as the boundary conditions at the surface, Y = 0. The flow properties at the downstream boundary, X = L, were also assumed to be constant along the X-direction. Therefore,

$$\frac{\partial f}{\partial X} = 0 \tag{7}$$

at X = L where f = $\rho$, U, V, and T.

The following procedures defined the far-field boundary conditions for a two-dimensional shock wave/turbulent boundary layer interaction flow field. The computational domain was chosen such that only the impinging oblique shock wave passed the far-field boundary (Y = H) and the reflected shock wave crossed the outflow boundary (X = L). The two-dimensional inviscid and adiabatic oblique shock wave theories were used to relate the flow properties upstream and downstream of the incoming shock wave. Conditions given in equations (6) and (7) were also imposed at the Y = 0 and X = L boundaries, respectively.

## RESULTS AND DISCUSSIONS

The previously described computational methods were used to obtain steady-state solutions of the density components, velocity components, and static temperature distributions within the two-dimensional shock wave/turbulent boundary layer interaction flows in references 3 and 4, and in Hingst and Porro's work (W.R. Hingst and A.R. Porro, NASA Lewis Research Center, Cleveland, Ohio, 1989, personal communication). On the basis of these flow properties, the static pressures, skin friction factors, and surface heat transfer rates were also determined. The computational results are described and compared with existing measurements in the following sections. Parameters such as the size of the physical domain L and H, the grid dimensions IM and JM, and the stretching factors $\lambda$ and $\beta$ which were chosen in the computations are also listed accordingly.

### Interaction Flow Fields at Mach 2.5

The flow properties were computed to predict some of the measurements in Hingst and Porro's work. This reference used a shock generator plate at 4° and 8° angles of attack to produce oblique shock waves in a Mach 2.5 free stream. The oblique shock wave impinged on the turbulent boundary layer along the wind tunnel wall. The experiments measured the surface pressure distributions for a near-adiabatic wall condition ($T_w/T_{0\infty}$ = 0.99) and measured the wall temperature distributions for a heated wall condition.

Initial Turbulent Boundary Layer. - Some of the computed properties of the turbulent boundary layer flow in Hingst and Porro's work are presented in figure 2. With the aid of the density profile and Crocco's relationship, Baronti and Libby (ref. 11) developed a compressible turbulent boundary layer flow analysis and found that the velocity in the boundary layer could be correlated in terms of two similarity laws - the law of the wall and the velocity defect law. Baronti and Libby's analysis and the measurements in

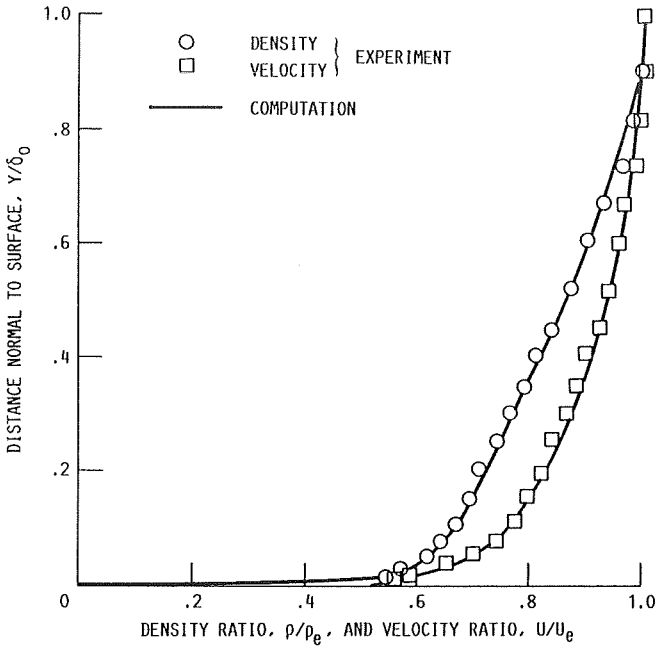


FIGURE 2. - DENSITY AND VELOCITY PROFILES IN COMPRESSIBLE TURBULENT BOUNDARY LAYER FLOW. SURFACE MACH NUMBER, $M_e$, 2.5; FREE-STREAM REYNOLDS NUMBER, $Re_{\delta_0}$, $0.53 \times 10^6$.

Hingst and Porro's work were used to investigate the accuracy of the present computed boundary layer flow properties. For this purpose, the density and the velocity profiles from Hingst and Porro's experiments and the present Navier-Stokes computations were used alternately in Baronti and Libby's analysis (ref. 11). By using the skin friction factor as a parameter, we could represent the velocity profiles in terms of the two similarity laws (fig. 3). A value of $C_{fo} = 0.0014$ was required to relate the experimental velocity profile to the similarity laws. The present Navier-Stokes computation predicted $C_{fo} = 0.0015$, which could also correlate the computational velocity profile in terms of the similarity laws. In addition, Navier-Stokes computation predicted a small surface heat transfer rate $Q_{wo} = 1.82 \times 10^3$ W/m$^2$ for the near-adiabatic wall condition.

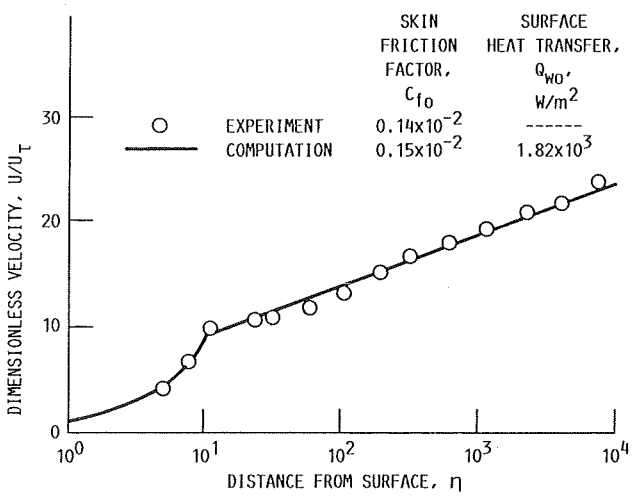


FIGURE 3. - TURBULENT BOUNDARY LAYER VELOCITY PROFILES IN TERMS OF SIMILARITY PARAMETERS $U/U_\tau$ AND $\eta$ (REF. 11). FREE-STREAM MACH NUMBER, $M_\infty$, 2.5.

Hingst and Porro also performed tests of the turbulent boundary layer for a heated wall condition. A section of the wall beneath the boundary layer was heated electrically at constant $Q_w$, and the surface temperatures along the heated surface were measured. For computational ease, the measured temperatures were used as the wall conditions. The Navier-Stokes computations of the turbulent boundary layer flow were repeated to calculate the surface heat transfer rates along the heated surface (fig. 4). The surface heat transfer rate increased gradually from the initial value $Q_{wo}$ to a constant value $Q_w = 7.15 \times 10^3$ W/m$^2$. This constant heat transfer rate is close to the heating rate $7.94 \times 10^3$ W/m$^2$ applied in the experiment. According to the previous observations, the present Navier-Stokes computations of the turbulent boundary layer flow could provide realistic initial flow conditions for the study of the shock wave/turbulent boundary layer interaction flows.

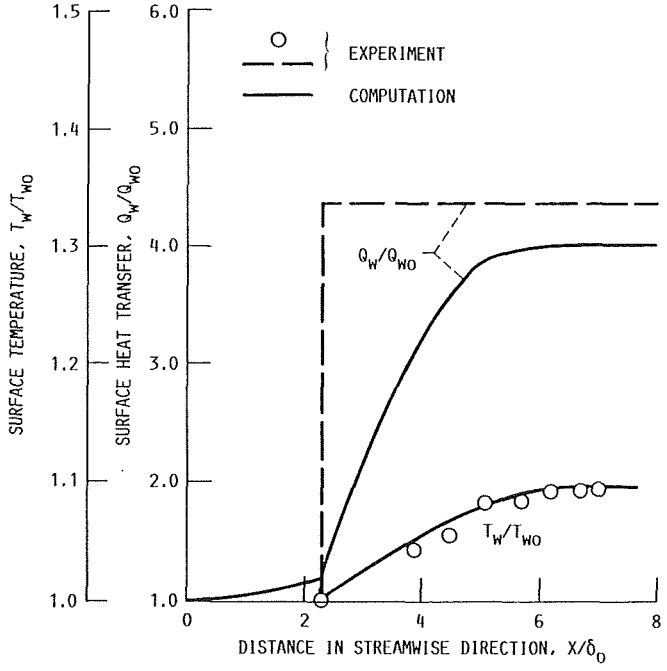


FIGURE 4. - SURFACE TEMPERATURE AND HEAT TRANSFER RATE OF A HEATED TURBULENT BOUNDARY LAYER FLOW. FREE-STREAM MACH NUMBER, $M_\infty$, 2.5; FREE-STREAM SURFACE HEAT TRANSFER RATE AT INITIAL CONDITIONS, $Q_{wo}$, $1.82 \times 10^3$ W/m$^2$; FREE-STREAM TEMPERATURE AT INITIAL CONDITIONS, $T_{wo}$, 290 K.

Shock Wave/Turbulent Boundary Layer Interaction. - By using the turbulent boundary layer flow properties as the initial conditions, we computed the flow properties within the oblique shock wave/turbulent boundary layer interaction flow fields in a Mach 2.5 free stream (W.R. Hingst and A.R. Porro, NASA Lewis Research Center, Cleveland, Ohio, 1989, personal communication). Figures 5, 6, 7, and 8 illustrate some results from these computations. Parameters related to the computations are also listed in figures 5 and 6 for reference.

The variations of the static pressure $p_w/p_\infty$ along the Y-direction at several $X/\delta_0$ locations are plotted in figures 5 and 6. The shock wave configurations were determined from these pressure data and were compared with the inviscid flow shock wave locations. The velocity boundary layer edge and the sonic line are also indicated in these figures. These figures show the

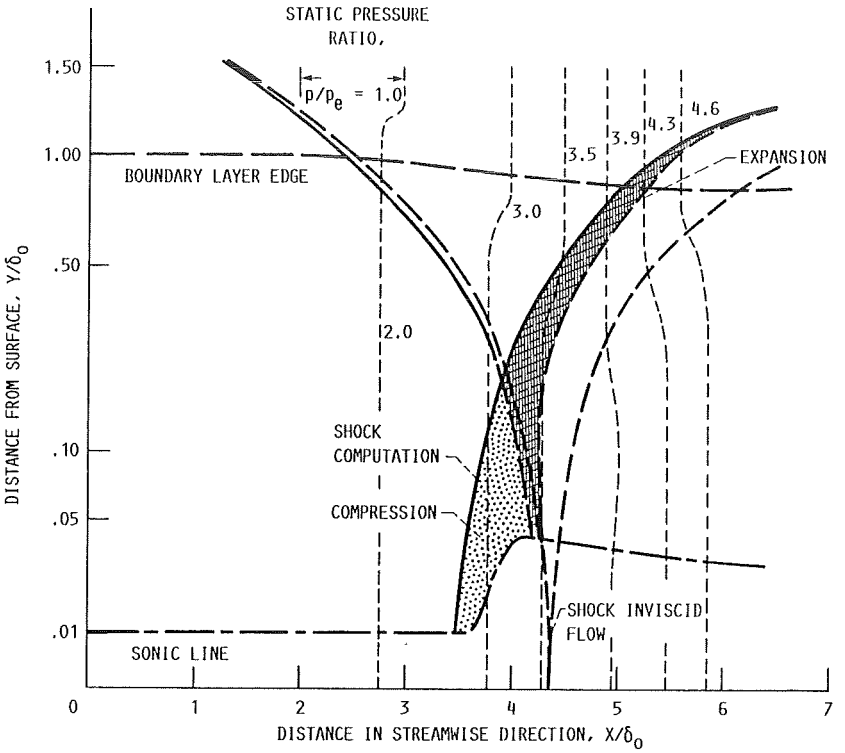


FIGURE 5. - WEAK INTERACTION FLOW. FREE-STREAM MACH NUMBER, $M_\infty$, 2.5; ANGLE OF ATTACK, $\theta$, $4^0$; GRID DIMENSIONS, IM, 221, AND JM, 119; STRETCHING FACTORS, $\lambda$, 5.0, AND $\beta$, 1.0012. NUMBERS REFER TO DIMENSIONLESS STREAMWISE DISTANCE, $x/\delta_0$, UNLESS INDICATED OTHERWISE.

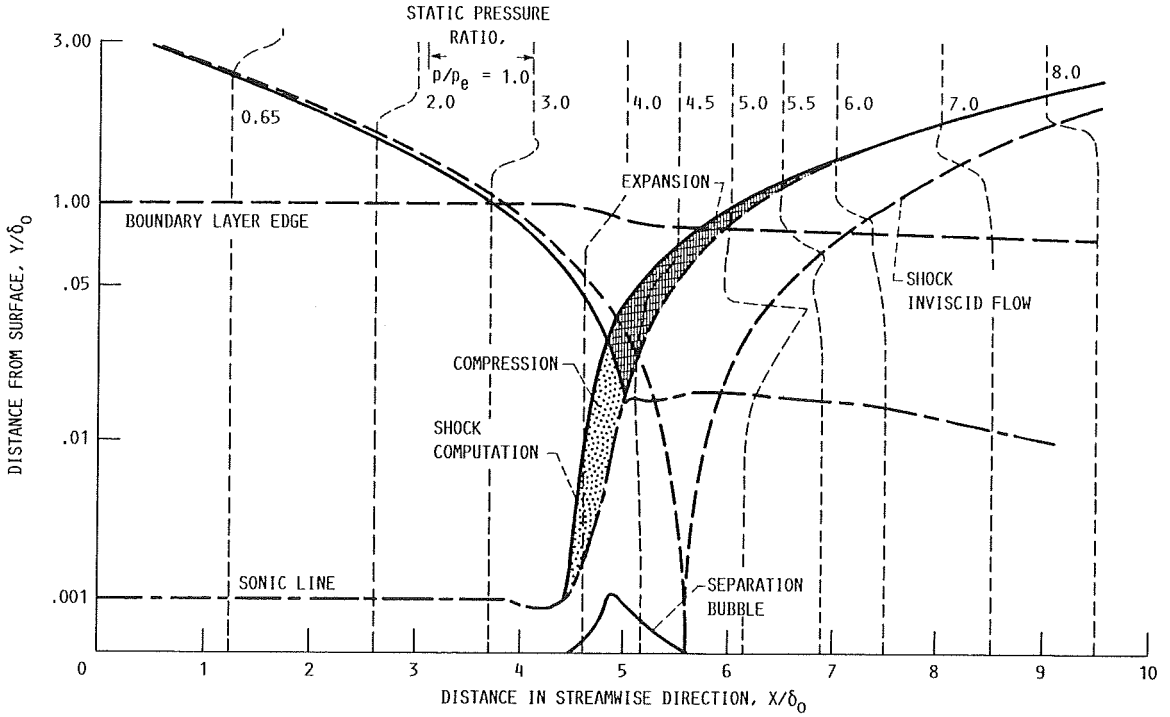


FIGURE 6. - STRONG INTERACTION FLOW. FREE-STREAM MACH NUMBER, $M_\infty$, 2.5; ANGLE OF ATTACK, $\theta$, $8^0$; GRID DIMENSIONS, IM, 221, AND JM, 119; STRETCHING FACTORS, $\lambda$, 5.0, AND $\beta$, 1.005. NUMBERS REFER TO DIMENSIONLESS STREAMWISE DISTANCE, $x/\delta_0$, UNLESS INDICATED OTHERWISE.

general characteristics of shock wave/boundary layer interaction flow fields. The subsonic layer was thickened and created compression waves which formed the shock wave in the upstream section of the interaction flow region. This shock wave interacted with the incoming oblique shock wave and the expansion waves due to the reduction of the subsonic layer thickness. The interaction formed the reflected shock wave which passed through the downstream boundary of the computational domain. These shock wave configurations indicated that the shock wave/turbulent boundary layer interaction had an upstream influence distance that was approximately equal to the initial boundary layer thickness.

The variations of surface pressure, skin friction factor, and surface heat transfer rate beneath the interaction flow are plotted in figures 7 and 8. The surface pressures are also compared with the measurements in Hingst and

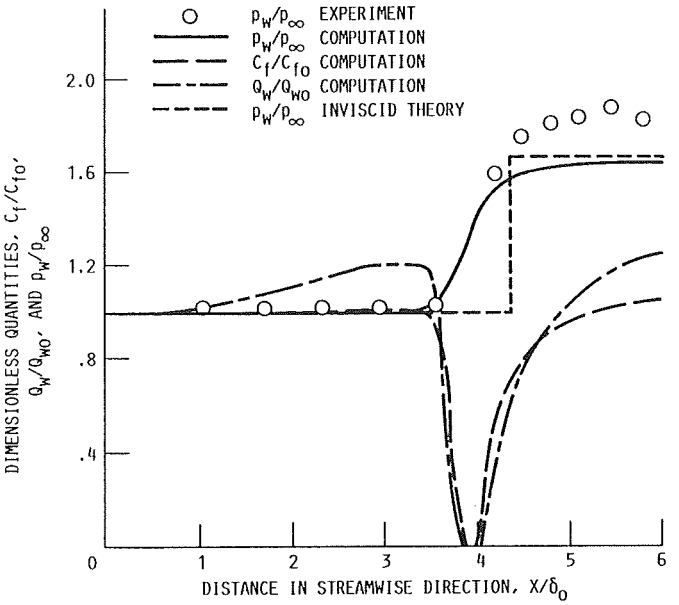


FIGURE 7. - SURFACE PRESSURE, $p_w/p_\infty$; SKIN FRICTION FACTOR, $C_f/C_{f_0}$; AND SURFACE HEAT TRANSFER RATE, $Q_w/Q_{w_0}$, IN WEAK INTERACTION FLOW. FREE-STREAM MACH NUMBER, $M_\infty$, 2.5; ANGLE OF ATTACK, $\theta$, $4^0$.

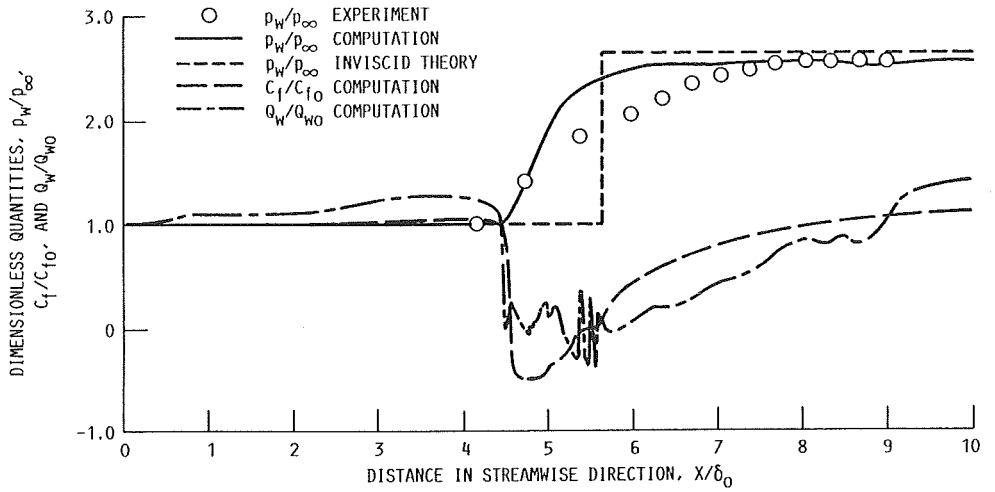


FIGURE 8. - SURFACE PRESSURE, $p_w/p_\infty$; SKIN FRICTION FACTOR, $C_f/C_{f_0}$; AND SURFACE HEAT TRANSFER RATE, $Q_w/Q_{w_0}$, IN STRONG INTERACTION FLOW. FREE-STREAM MACH NUMBER, $M_\infty$, 2.5; ANGLE OF ATTACK, $\theta$, $8^0$.

Porro's work. The present computations predicted a lower surface pressure level with a wedge angle of 4° and a higher surface pressure level with a wedge angle of 8°. The skin friction factor remained approximately at the initial value before the local surface pressure increased. When the surface pressure increased, the skin friction factor decreased and then increased to a value approximately the same as its initial value. With the free-stream conditions, the oblique shock wave with $\Theta = 4°$ induced a weak interaction which did not separate the boundary layer in the interaction flow region. However, the shock wave with $\Theta = 8°$ induced a strong interaction which caused a small separation bubble within the interaction flow field. The surface heat transfer rate changed in a pattern similar to that of the skin friction. However, the oblique shock wave induced an increase in the surface heat transfer rates at the upstream locations where the skin friction factors and surface pressures remained the same as the initial conditions. With the strong shock wave interaction, the surface heat transfer rate at the downstream locations did not recover its initial value as quickly as it did in the weak shock wave interaction flow field.

**Interaction Flow Fields at Mach 6**

Alzner and Zakkay (ref. 3) and Zakkay and Wang (ref. 4) performed experiments to probe the flow fields of oblique shock wave/turbulent boundary layer interaction with Mach 6 free-stream conditions. The experiments were performed with a cold wall ($T_w/T_{0\infty} = 0.66$) condition. The static pressure, pitot pressure, total temperature, and surface heat transfer rate within the interaction flow field were measured. These measurements could verify the Navier-Stokes calculations of the properties of a shock wave/turbulent boundary layer interaction flow with a high free-stream Mach number condition. The present authors also used the computational methods to predict some of the measurements in references 3 and 4. The results are described in the following section.

Initial Turbulent Boundary Layer. - Similar to the study in the Initial Turbulent Boundary Layer portion of the section **Interaction Flow Fields at Mach 2.5**, the Navier-Stokes computational code and Baronti and Libby's analysis were used to predict the initial turbulent boundary layer properties. The measurements in references 3 and 4 were used in the boundary layer flow analysis. Some of the results are shown in figures 9 and 10. The skin friction factors and surface heat transfer rates obtained from the analyses and experiments are also listed and compared in these figures. Excellent agreement between the results from the analyses and experiments was found.

Shock Wave/Turbulent Boundary Layer Interactions. - In the experiments by Alzner and Zakkay (ref. 3), the boundary layer developed along an axisymmetric centerbody in a Mach 6 free stream. An axisymmetric wedge (10° wedge angle) was inserted in the free stream to induce an oblique shock wave. The shock wave impinged on the turbulent boundary layer and a shock wave/turbulent boundary layer interaction flow occurred. The present computational procedures were performed to predict the properties within this interaction flow field. Some of the computational results are shown in figures 11 and 12. Parameters used in the computational scheme are also listed in figure 11.

The static pressure $p_w/p_\infty$ variations along the Y-direction at several $X/\delta_0$ locations are plotted in figure 11. From the pressure variations, the

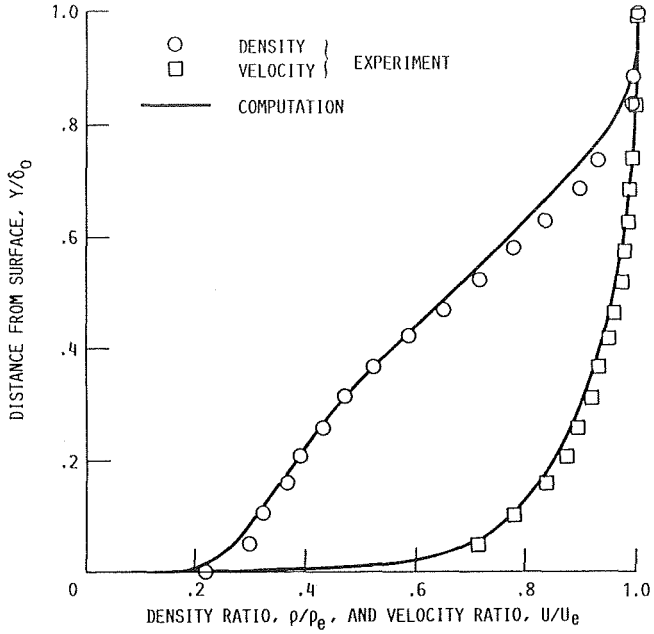


FIGURE 9. - DENSITY AND VELOCITY PROFILES IN TURBULENT BOUNDARY LAYER FLOW. FREE-STREAM MACH NUMBER, $M_\infty$, 6.0; FREE-STREAM REYNOLDS NUMBER, $Re_{\delta o}$, $3.75 \times 10^6$.

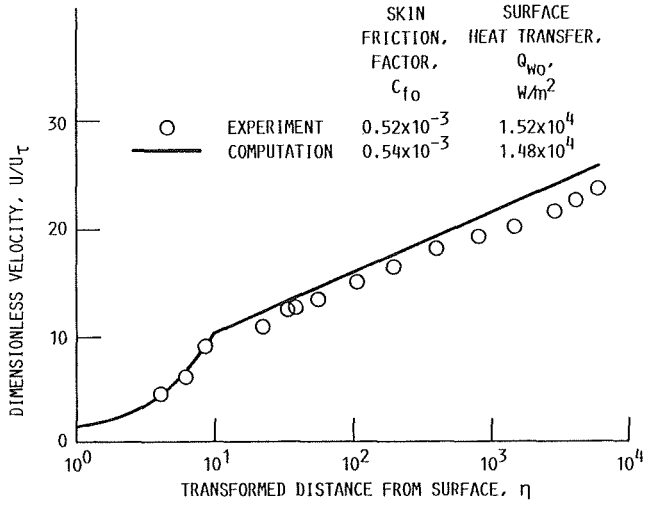


FIGURE 10. - TURBULENT BOUNDARY LAYER VELOCITY PROFILES IN TERMS OF SIMILARITY PARAMETERS $U/U_\tau$ AND $\eta$ (REF. 11). FREE-STREAM MACH NUMBER, $M_\infty$, 6.0

shock wave configurations, compression wave regions, and expansion wave regions were determined. These are shown in figure 11 together with the boundary layer edge and the sonic line locations. The variations of the surface pressure $p_w/p_\infty$, skin friction factor $C_f/C_{fo}$, and surface heat transfer rate $Q_w/Q_{wo}$ are shown in figure 12. The skin friction factor plot indicates that the flow separated at $X/\delta_o = 4.90$ and then reattached to the surface at $X/\delta_o = 5.50$. The surface heat transfer rate increased at upstream locations where the surface pressure and skin friction factor remained the same as the initial conditions. With the cold wall condition $T_w/T_{o\infty} = 0.66$, the surface heat transfer rate increased within the separated flow region and continued to increase after the flow reattached to the surface.

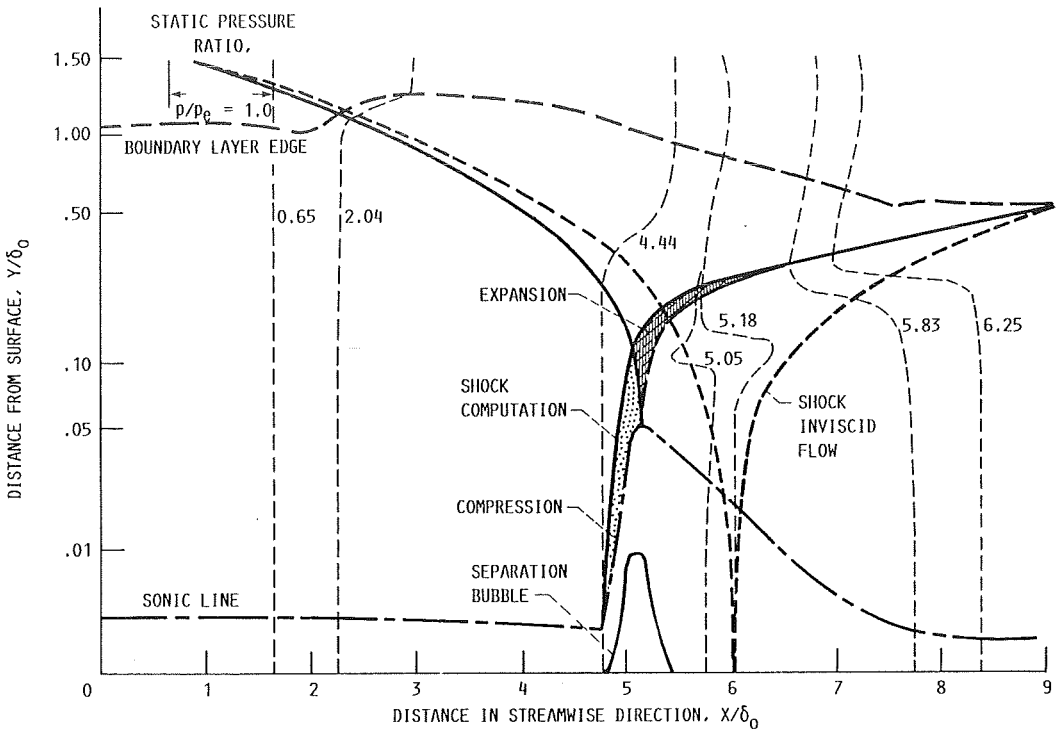


FIGURE 11. - STRONG INTERACTION FLOW. FREE-STREAM MACH NUMBER, $M_\infty$, 6.0; ANGLE OF ATTACK, $\theta$, $10^0$; GRID DIMENSIONS, IM, 221, AND JM, 119; STRETCHING FACTORS, $\lambda$, 5.0, AND $\beta$, 1.0026. NUMBERS REFER TO DIMENSIONLESS STREAMWISE DISTANCE, $x/\delta_0$, UNLESS INDICATED OTHERWISE.

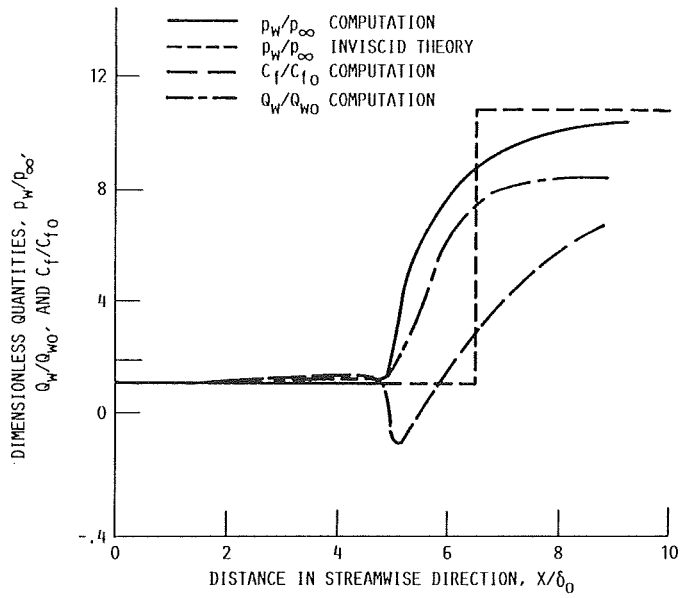


FIGURE 12. - SURFACE PRESSURE, $p_w/p_\infty$; SKIN FRICTION FACTOR, $C_f/C_{fo}$, AND SURFACE HEAT TRANSFER RATE, $Q_w/Q_{wo}$, IN STRONG INTERACTION FLOW. FREE-STREAM MACH NUMBER, $M_\infty$, 6.0; ANGLE OF ATTACK, $\theta$, $10^0$; FREE-STREAM REYNOLDS NUMBER, $Re_{\delta_0}$, $2.68 \times 10^6$.

Zakkay and Wang (ref. 4) also performed a shock wave/turbulent boundary layer interaction flow experiment in a Mach 6 free stream. An axisymmetric cowl (approximately 4° wedge angle) with a gradual turning angle was inserted in the test section of a Mach 6 blow-down wind tunnel facility to produce a longitudinal adverse pressure gradient in the free stream. The turbulent

boundary layer developed along the surface of a streamlined axisymmetric centerbody passing through the entire length of the wind tunnel nozzle. Thereby, the boundary layer was subjected to an adverse pressure gradient induced by the compression cowl. The adverse pressure gradient extended downstream for a distance of approximately 10 times the initial boundary layer thickness. The experiment measured the static pressure, pitot pressure, and total temperature profiles within the interaction flow region. The surface heat transfer rates were also measured with the cold wall condition. This experimental data could be used to verify the Navier-Stokes computations of the realistic shock wave/turbulent boundary layer interaction flow properties. Therefore, the present numerical computations were also performed to study the experimental results. Figure 13 shows the schematics of the flow field in the physical domain and the limited region for the computations. Parameters chosen for the computational scheme were also listed for reference.

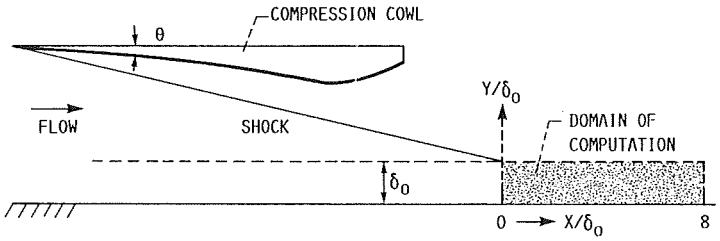


FIGURE 13. - WEAK INTERACTION FLOW WITH COMPRESSION COWL. FREE-STREAM MACH NUMBER, $M_\infty$, 6.0; ANGLE OF ATTACK, θ, $4^0$; GRID DIMENSIONS, IM, 251, AND JM, 58; STRETCHING FACTORS, λ, 5.0, AND β, 1.0017.

Because of the complex flow field, the initial and boundary conditions for the computations were specified differently from those described in the computation method section of this paper. The initial conditions at $X = 0$ were calculated by using the Navier-Stokes code. The experimental profiles (ref. 4) of the static pressure, pitot pressure, and total temperature were first used to determine preliminary profiles of $\rho$, U, V, and T at the initial station. These preliminary profiles were chosen as the initial profiles in the Navier-Stokes code, and the code was executed with a coarse grid in the X-direction. The computation was repeated by iterating the initial profiles until it gave static pressures and pitot pressures at $X = 0$ which were compatible to the measurements in reference 4. A surface heat transfer rate $Q_{wo} = 2.61 \times 10^3$ W/m$^2$ and a skin friction factor $C_{fo} = 0.00052$ were computed, and they agreed well with their values reported in reference 4.

The far-field boundary conditions were also required in the iteration process. These far-field boundary conditions were obtained by matching the static pressures and pitot pressures at $Y = H$. From the previously described coarse grid iteration process, an approximately constant static pressure was found along the Y-direction at the initial station ($X = 0$). By using this static pressure as the downstream static pressure of an oblique shock wave induced by a 3.5° wedge in a Mach 6 free stream, the inviscid flow relations gave a pitot pressure close to that which was measured in reference 4. Thus, the present computational domain was within the downstream side of the oblique shock wave induced by the compression cowl lip. To determine the far-field boundary conditions, we assumed the total pressure to be constant at $Y = H$. On the basis of the ratio of the pitot pressures (ref. 4) and total pressure, the Mach number and the static pressure at any location (X,H) were determined from the inviscid flow theory. The velocity components U and V were then obtained from the inviscid Prandtl-Meyer simple wave relation. The adiabatic

flow condition was also assumed at $Y = H$ to define the far-field static temperatures. Some of these far-field boundary conditions are shown in figure 14.

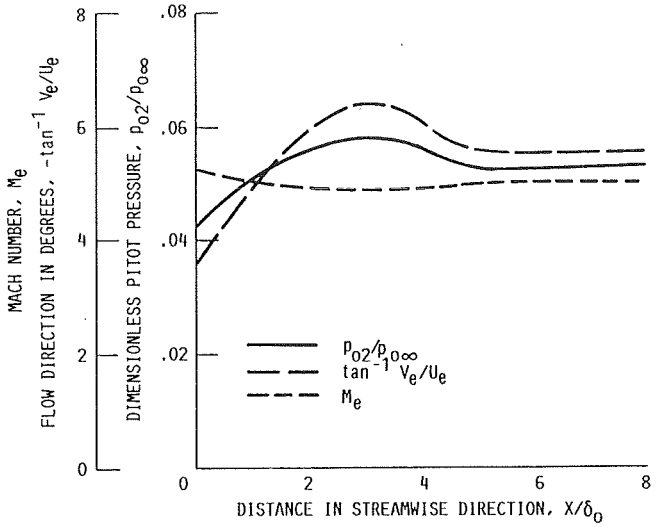


FIGURE 14. - FAR-FIELD BOUNDARY CONDITIONS OF WEAK INTERACTION FLOW. FREE-STREAM MACH NUMBER, $M_\infty$, 6.0; FREE-STREAM REYNOLDS NUMBER, $Re_{\delta_0}$, $3.75 \times 10^6$.

With the initial conditions and the far-field boundary conditions given previously, the Navier-Stokes computations of the interaction flow were executed again by using a fine grid in the X-direction. The computational results of the static pressures and the pitot pressures along the Y-direction at three $X/\delta_0$ locations were shown in figures 15 and 16, and they were also compared with the measurements in reference 4. These computations predicted the general patterns of the experimental static and pitot pressure variations. The computations did not indicate flow separation within the interaction flow region. The surface pressure and the surface heat transfer rate variations are shown in figure 17. These computations also approximated the experimental surface pressure and heat transfer rate.

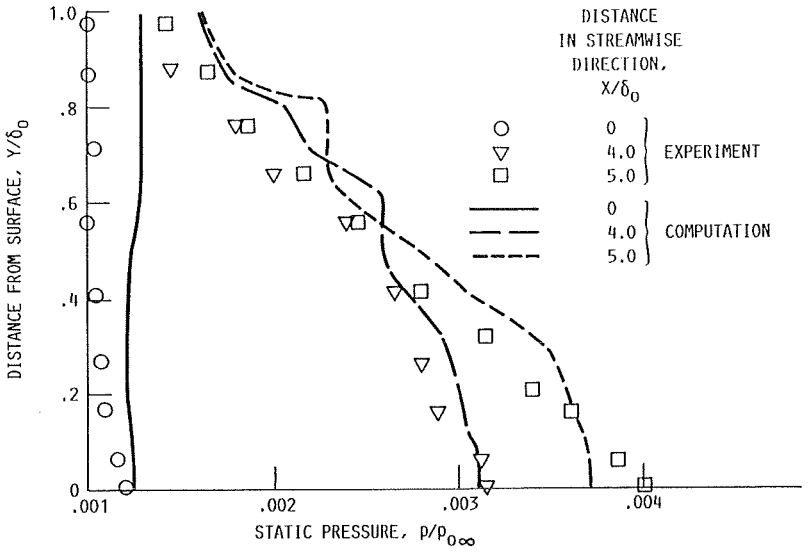


FIGURE 15. - COMPARISON OF STATIC PRESSURE PROFILES IN WEAK INTERACTION FLOW. FREE-STREAM MACH NUMBER, $M_\infty$, 6.0.

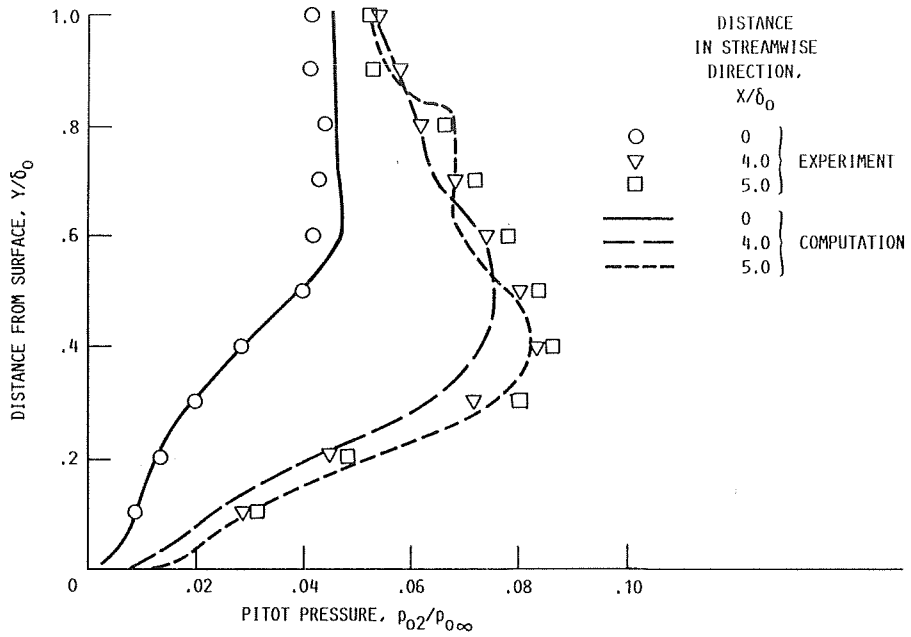


FIGURE 16. - COMPARISON OF PITOT PRESSURES IN WEAK INTERACTION FLOW. FREE-STREAM MACH NUMBER, $M_\infty$, 6.0.

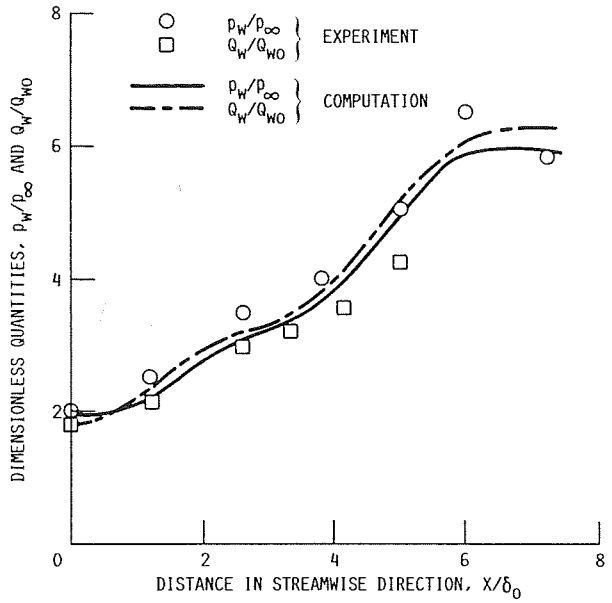


FIGURE 17. - SURFACE PRESSURE, $p_w/p_\infty$, AND HEAT TRANSFER, $Q_w/Q_{wo}$, BENEATH WEAK INTERACTION FLOW. FREE-STREAM MACH NUMBER, $M_\infty$, 6.0.

## Surface Heat Transfer and Pressure Correlation

Holden (ref. 8) suggested that, within a supersonic or hypersonic shock wave/turbulent boundary layer interaction flow field, local surface pressure and heat transfer rate could be correlated by

$$\frac{Q_w}{Q_r} = \left(\frac{p_w}{p_r}\right)^{0.85} \tag{8}$$

where $P_r$ and $Q_r$ are the reference pressure and reference heat transfer rate, respectively. This relationship was studied here by using the present computational results of the Mach 6 interaction flow fields.

The surface pressures and heat transfer rates calculated in the two cases of Mach 6 interaction flow fields were normalized respectively with the free-stream static pressure and the turbulent boundary layer heat transfer rate. These two dimensionless quantities, $Q_w/Q_{wo}$ and $p_w/p_\infty$, are correlated in figure 18. The measurements of the surface pressures and heat transfer rates are also normalized and correlated in figure 18 for comparison. The comparison indicates that equation (8) correlated reasonably with the surface heat transfer rates and pressures when the flow did not separate in the interaction flow field. When flow separation occurred, equation (8) predicted a higher surface heat transfer rate than that obtained from the present computations. After the reattachment point, the computation showed that the surface pressure and heat transfer rate recovered the relationship given by equation (8).

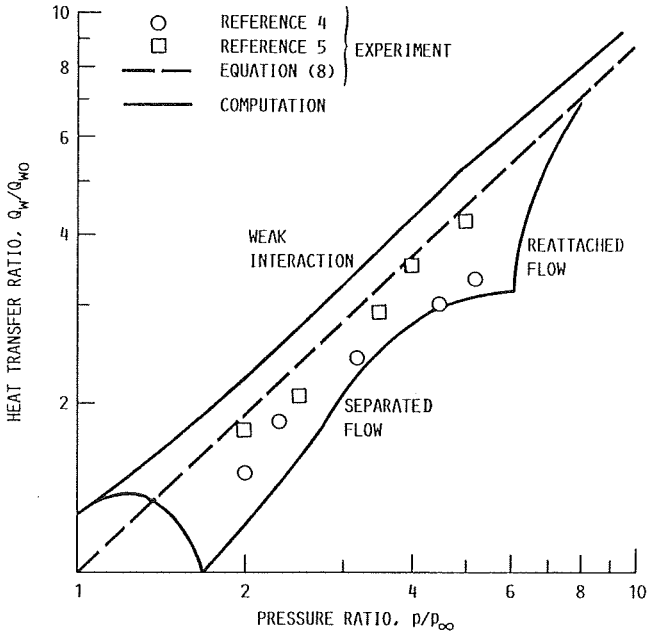


FIGURE 18. - SURFACE PRESSURE AND HEAT TRANSFER CORRELATIONS IN INTERACTION FLOW. FREE-STREAM MACH NUMBER, $M_\infty$, 6.0.

The shock wave impingement increased the surface heat transfer rate at locations upstream of the interaction flow field (figs. 7 and 8). By using this upstream surface heat transfer rate as the reference value, we could reduce the normalized heat transfer rate and correlate it closely with equation (8). It is also interesting to see in figure 18 that the present Navier-Stokes computations predicted surface pressure/heat transfer correlations which enclosed the experimental data in references 3 and 4.

## Velocity-Temperature Correlations

Crocco's velocity-temperature relationship equation (5) has been an important part of the compressible turbulent boundary layer flow study. There are certain conditions (such as the requirements of adiabatic wall condition

with a streamwise pressure gradient or the requirement that the pressure and wall temperatures be constant with surface heat transfer) which restricted the use of Crocco's relationship. The present computations provided U and T data to study the validity of using equation (5) in a shock wave/turbulent boundary layer interaction flow field.

From the present computations of the interaction flow fields, the dimensionless quantities $U/U_e$ and $T/T_e$ were calculated at locations along the Y-direction at different $X/\delta_o$ stations. Equation (5) was also used to determine $T/T_e$ as functions of the far-field conditions and $U/U_e$. A recovery factor $\gamma = 0.9$ was used in equation (5). The resulting $T/T_e$ from these two approaches are plotted as functions of $U/U_e$ in figures 19 to 22. For near-adiabatic wall conditions (figs. 19 and 20), equation (5) correlated well the computational results of $T/T_e$ and $U/U_e$ within the unseparated flow region. For the cold wall condition at Mach 6, equation (5) correlated approximately with the computational results (figs. 21 and 22) when there was no flow separation. When flow separation occurred, equation (5) could

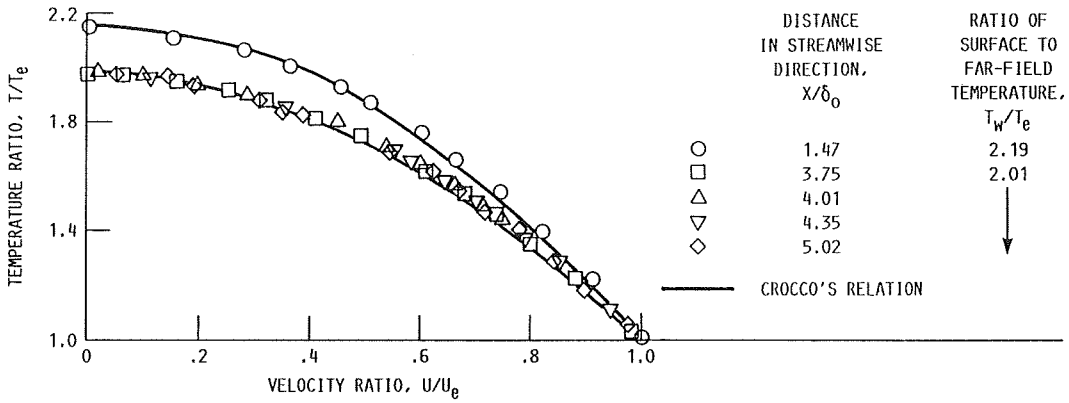


FIGURE 19. - VELOCITY-TEMPERATURE CORRELATIONS IN WEAK INTERACTION FLOW WITH NEAR-ADIABATIC SURFACE TEMPERATURES. FREE-STREAM MACH NUMBER, $M_\infty$, 2.5; ANGLE OF ATTACK, $\theta$, $4^o$.

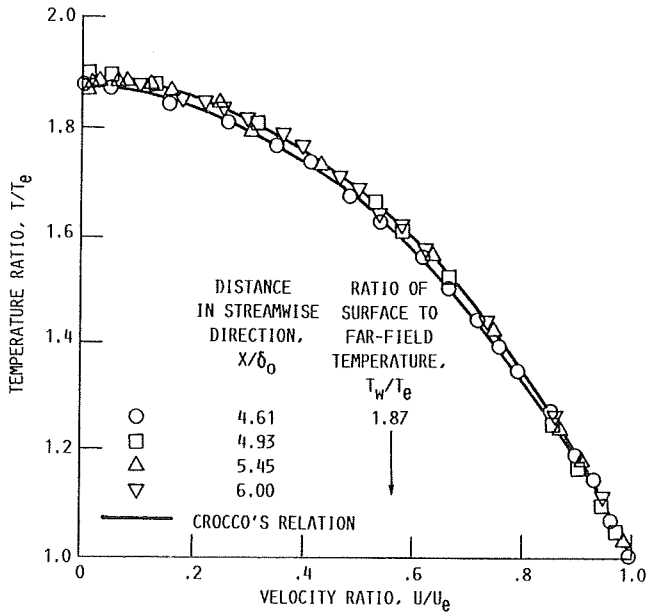


FIGURE 20. - VELOCITY-TEMPERATURE CORRELATIONS IN STRONG INTERACTION FLOW WITH NEAR-ADIABATIC SURFACE TEMPERATURE. FREE-STREAM MACH NUMBER, $M\infty$, 2.5; ANGLE OF ATTACK, $\theta$, $8^o$.

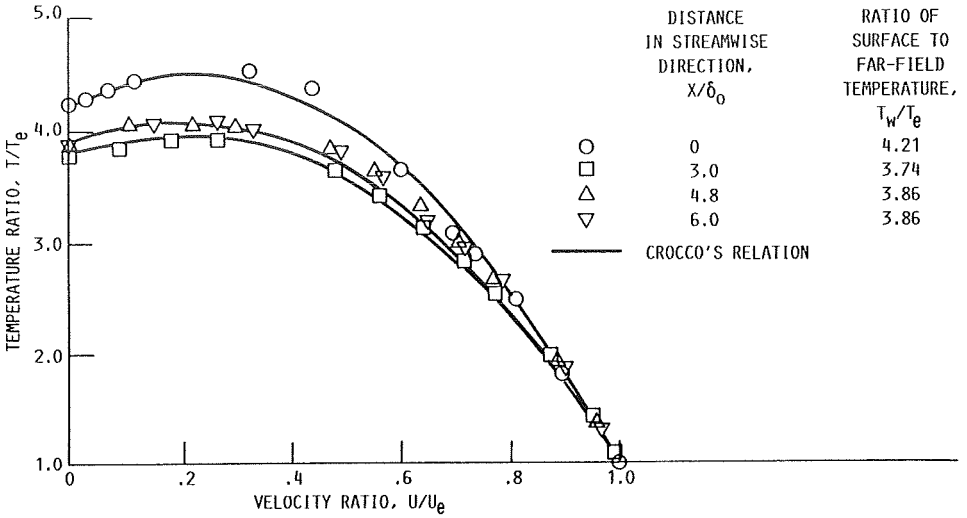


FIGURE 21. - VELOCITY-TEMPERATURE CORRELATIONS IN WEAK INTERACTION FLOW WITH COOLED-WALL CONDITION. FREE-STREAM MACH NUMBER, $M_\infty$, 2.5.

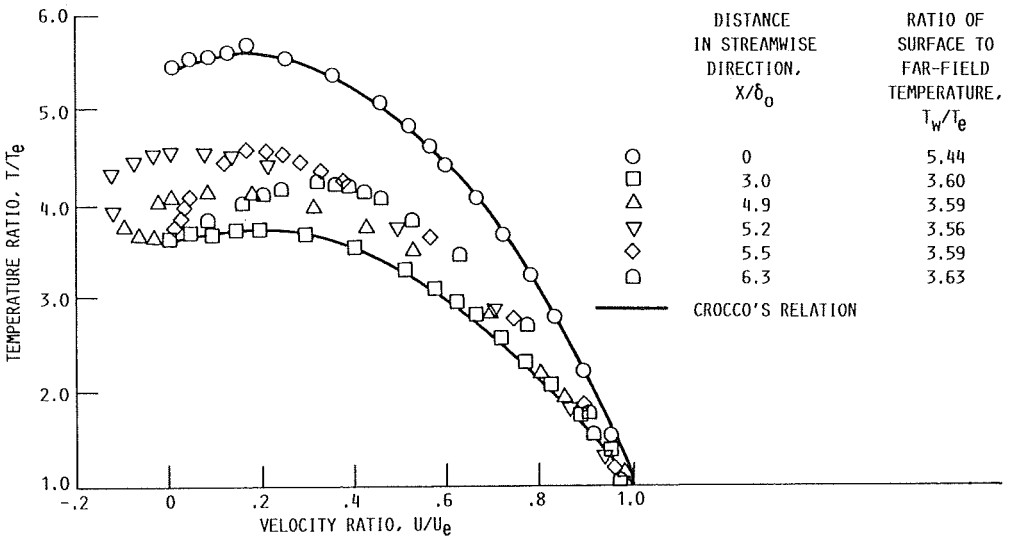


FIGURE 22. - VELOCITY-TEMPERATURE CORRELATIONS IN STRONG INTERACTION FLOW WITH COOLED-WALL CONDITION. FREE-STREAM MACH NUMBER, $M_\infty$, 6.

correlate only the $U/U_e$ and $T/T_e$ within the upstream section of the flow field, and it failed to correlate the $U/U_e$ and $T/T_e$ within the flow region after the location of flow separation. However, the results of $U/U_e$ and $T/T_e$ from the Navier-Stokes computations showed a tendency to regain Crocco's relationship within the reattachment flow region.

## Turbulent Shear Stress

The Baldwin-Lomax turbulence model was used to represent the turbulence transport in the present interaction flow computation. It is an algebraic turbulence model which assumes different growth rates of eddy viscosity for inner and outer layers. This model did not require the determination of the boundary layer edge and was convenient for Navier-Stokes computations. Since the empirical constants were chosen by its agreement with the turbulence level for a constant pressure boundary layer at transonic speed, the use of this model outside of the domain of its empirical base should be examined further. Rose and Johnson (ref. 6) measured the Reynolds shear stresses in a shock

wave/turbulent boundary layer interaction flow in a Mach 2.9 free stream. Their data could be used to verify the use of the Baldwin-Lomax turbulence model in an interaction flow field. As a first step in this direction, the ability of the Baldwin-Lomax turbulence model to calculate the Reynolds shear stresses within a supersonic turbulent boundary layer flow was also investigated in this study.

In this study, the mean flow properties of the Mach 2.9 turbulent boundary layer flow in reference 6 were calculated by following the methods in the section Initial Conditions (of the Computational Methods section). These mean flow properties and the turbulence model were used to determine the Reynolds shear stresses $-\rho\overline{u'v'}$. A similar computational process was used to define the Reynolds shear stresses within the Mach 6 turbulent boundary layer. The Reynolds stress computations were repeated with different values of $C_{cp}$. Maise and McDonald (ref. 12) also showed that within the Mach number range of 0 to 5 the effect of compressibility on the normalized shear stress was quite small and was in keeping with Morkovin's hypothesis (ref. 13). The present Reynolds shear stress computations were also studied for the Mach number effect on Baldwin-Lomax turbulence modeling. The computational results of $-\rho\overline{u'v'}$ were normalized with $-\rho U_e^2/2$ to obtain the dimensionless quantity $-2\overline{u'v'}/U_e^2$. Both $-\rho\overline{u'v'}$ and $-2\overline{u'v'}/U_e^2$ are plotted and compared with Klebanoff's results (ref. 14) of $-2\overline{u'v'}/U_e^2$ in an incompressible turbulent boundary layer flow in figures 23 and 24. The corresponding Reynolds stress measurements are also shown in figure 23.

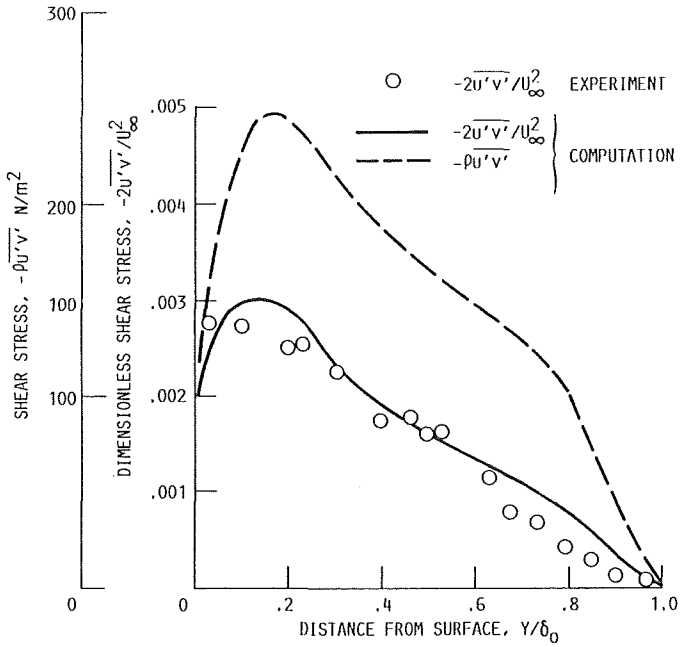


FIGURE 23. - REYNOLDS SHEAR STRESS IN TURBULENT BOUNDARY LAYER. FREE-STREAM MACH NUMBER, $M_\infty$, 2.9; FREE-STREAM REYNOLDS NUMBER, $Re_{\delta_0}$, $1.4\times10^6$, TURBULENCE CONSTANT, $C_{cp}$, 2.0. SKIN FRICTION FACTOR, $C_{f_0}$; FOR EXPERIMENT, $0.10\times10^{-2}$; FOR COMPUTATION, $0.93\times10^{-3}$; SURFACE HEAT TRANSFER FOR COMPUTATION, $Q_{w_0}$, $0.45\times10^3$ W/m$^2$.

Assuming that the Mach number effect on $-2\overline{u'v'}/U^2$ is negligible and that $-2\overline{u'v'}/U_e^2$ in a compressible turbulent boundary layer should agree with the

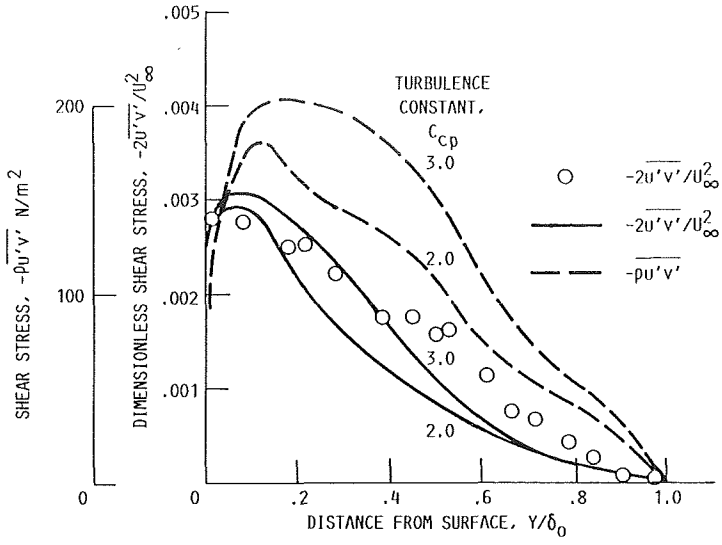


FIGURE 24. - REYNOLDS SHEAR STRESS IN TURBULENT BOUNDARY LAYER. FREE-STREAM MACH NUMBER, $M_\infty$, 6.0; FREE-STREAM REYNOLDS NUMBER, $Re_{\delta_0}$, $2.7 \times 10^6$. SKIN FRICTION FRACTOR, $C_{f_0}$; FOR EXPERIMENT, $0.52 \times 10^{-3}$; FOR COMPUTATION, $0.56 \times 10^{-3}$; SURFACE HEAT TRANSFER, $Q_{w_0}$: FOR EXPERIMENT, $1.48 \times 10^4$ W/m$^2$ ; FOR COMPUTATION, $1.54 \times 10^4$ W/m$^2$.

same parameter in an incompressible boundary layer, the results in figures 23 and 24 indicate that different $C_{cp}$ values are required in Baldwin-Lomax turbulence modeling. Figure 23 indicates that $C_{cp} = 2.0$ was required for the Mach 2.9 turbulent boundary layer flow, and this $C_{cp}$ value was used in the present computations. Figure 24 shows that $C_{cp} = 3.0$ was required for a Mach 6 turbulent boundary layer. Without additional modification of the inner layer assumption of the Baldwin-Lomax turbulence modeling, the present Navier-Stokes computations could predict the skin friction factor and surface heat transfer rate beneath a compressible turbulent boundary layer flow.

The present computational methods were also used to determine the turbulent shear stress properties of the shock wave/turbulent boundary layer interaction flow in reference 6. The Baldwin-Lomax turbulence model with $C_{cp} = 2.0$ was used to represent the turbulence transport, and the turbulent shear stresses $-\rho u'v'$ within the interaction flow were calculated. The computational results of the turbulent shear stress profiles at three different $X/\delta_0$ locations are plotted in figure 25. They are also compared with the measurements in reference 6. Both the computational and experimental results show that $-\rho u'v'$ decreased in the upstream section ($X/\delta_0 < 1.8$) and then increased greatly in the downstream region ($X/\delta_0 \geq 5.0$) of the interaction flow field. However, the computational results of $-\rho u'v'$ were larger than the measurements in reference 6. This discrepancy is being investigated.

Experimental analyses of the Reynolds stresses within a shock wave/ turbulent boundary layer interaction flow have been reported in some recent studies (refs. 15 and 16). Debieve and Lachame (ref. 15) found that turbulence amplified along a streamline after it crossed a shock wave. Ha Minh and Vandromme (ref. 17) argued that a mixing length turbulence model might not represent the features of turbulence in a shock wave/turbulent boundary layer interaction flow field, and they suggested using the mass-averaged forms of the Reynolds stress equations for the turbulence modeling in Navier-Stokes equations. An analysis was developed by Debieve, Gouin, and Gaviglio (ref. 16)

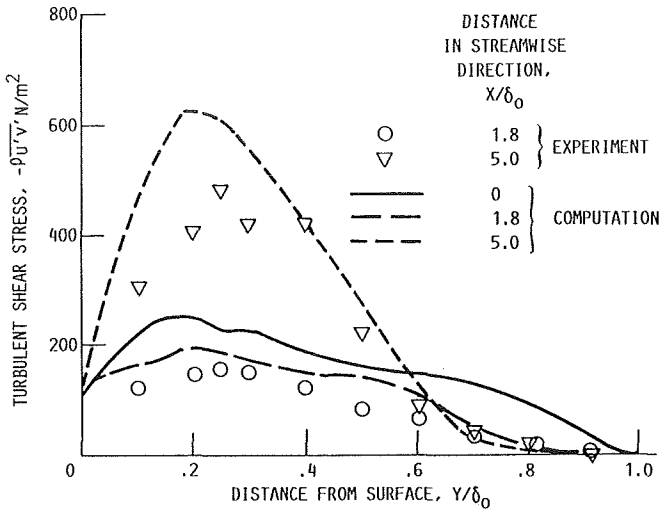


FIGURE 25. - TURBULENT SHEAR STRESSES WITHIN A SHOCK WAVE/ TURBULENT BOUNDRY LAYER INTERACTION REGION.

to relate the mean flow and Reynolds stress tensor evolution in a shock wave/ turbulent boundary layer interaction flow. The applications of this Reynolds stress analysis in the Navier-Stokes computations of the shock wave/turbulent boundary layer interaction flows will be pursued in the near future.

## CONCLUSIONS

Numerical computations of Navier-Stokes equations were performed to predict the flow properties within two-dimensional shock wave/turbulent boundary layer interaction flows in Mach 2.5 and 6.0 free streams. The interaction flow fields due to oblique shock wave impingement on a turbulent boundary layer over a flat surface with near-adiabatic ($T_w/T_{o\infty}$ = 0.99) and cold wall ($T_w/T_{o\infty}$ = 0.66) conditions were considered. To minimize the effect of initial conditions on the computations, we calculated the initial turbulent boundary layer properties to ensure that the initial boundary layer velocity and temperature profiles gave the correct skin friction factor and surface heat transfer rate. The computational results were analyzed to study the surface heat transfer rate, velocity-temperature correlation, and turbulent shear stress within the interaction flow fields. These computational results were also compared with existing measurements.

This present study indicates that

1. With the prescribed surface temperature conditions, the shock wave impingement increased the surface heat transfer rate in the upstream section of the interaction flow field, whereas the surface pressure and skin friction remained the same as those of the incoming turbulent boundary layer.

2. With a near-adiabatic surface, the surface heat transfer rate changed in a pattern similar to that of the skin friction within both the weak and strong interaction flow fields.

3. With a weak shock wave interaction over a cold wall, the surface heat transfer rate increased continuously in the downstream direction, and the local surface heat transfer rate and pressure could be correlated with Holden's relationship. With a strong shock wave interaction over a cold wall,

the local surface heat transfer rate also increased but was lower than that predicted by Holden's relationship.

4. With a near-adiabatic surface, Crocco's relationship could correlate the mean flow streamwise velocity components and static temperatures in a weak interaction flow field and in the unseparated region of a strong interaction flow field. For a cold wall condition, Crocco's relationship could only correlate the mean flow streamwise velocity components and static temperature in a weak interaction flow field.

5. When the Baldwin-Lomax turbulence model was used, the Navier-Stokes computations predicted qualitatively the turbulent shear stress $-\rho\overline{u'v'}$ in shock wave/turbulent boundary layer interaction flows. The Baldwin-Lomax turbulence model might require modification in order to represent the turbulence transport in the Navier-Stokes computations of the interaction flows with different free-stream Mach numbers.

This study used simple two-dimensional forms of the Navier-Stokes equations to simulate the complicated shock wave/turbulent boundary layer interaction flow. The radius of curvature in the axisymmetric cases and the three-dimensionality due to flow separation were not considered. However, the present computational results might have indicated that, with proper inflow conditions, an improved Navier-Stokes numerical computational code could calculate the surface heat transfer rates within a shock wave/turbulent boundary layer interaction flow.

## REFERENCES


1. Delery, J.; Marvin, J.G.; and Reshotko, E.: Shock-Wave Boundary Layer Interactions. AGARD AG-280, 1986.

2. Shang, J.S.; Hankey, W.L.; and Law, C.H.: Numerical Simulation of Shock Wave-Turbulent Boundary Layer Interaction. AIAA J., vol. 14, no. 10, Oct. 1976, pp. 1451-1457.

3. Alzner, E.; and Zakkay, V.: Turbulent Boundary-Layer Shock Interaction With and Without Injection. AIAA J., vol. 9, no. 9, Sept. 1971, pp. 1760-1771.

4. Zakkay, V.; and Wang, C.R.: Turbulent Boundary Layer in an Adverse Pressure Gradient Without Effect of Wall Curvature. NASA CR-112247, 1972.

5. Baldwin, B.; and Lomax, H.: Thin-Layer Approximation and Algebraic Model for Separated Turbulent Flows. AIAA Paper 78-257, Jan. 1978.

6. Rose, W.C.; and Johnson, D.A.; Turbulence in a Shock-Wave Boundary Layer Interaction. AIAA J., vol. 13, no. 7, July 1975, pp. 884-889.

7. Fernholz, H.H.: A Critical Commentary on Mean Flow Data for Two-Dimensional Compressible Turbulent Boundary Layers. AGARD AG-253, 1980.

8. Holden, M.S.: Shock Wave-Turbulent Boundary Layer Interaction in Hypersonic Flow. AIAA Paper 77-45, Jan. 1977.

9. MacCormack, R.W.: The Effect of Viscosity in Hypervelocity Impact Cratering. AIAA Paper 69-354, Apr. 1969.

10. Anderson, D.A.; Tannehill, J.C.; and Pletcher, R.H.: Computational Fluid Mechanics and Heat Transfer. McGraw-Hill, 1984.

11. Baronti, P.O.; and Libby, P.A.; Velocity Profiles in Turbulent Compressible Boundary Layers. AIAA J., vol. 4, no. 2, Feb. 1966, pp. 193-194.

12. Maise, G.; and McDonald, H.: Mixing Length and Kinematic Eddy Viscosity in a Compressible Boundary Layer. AIAA J., vol. 6, no. 1, Jan. 1968, pp. 73-74.

13. Morkovin, M.U.: Effects of Compressibility on Turbulent Flows. Mechanics of Turbulence. Gordon and Breach Science Publishers, 1964, pp. 367-380.

14. Klebanoff, P.S.: Characteristics of Turbulence in a Boundary Layer With Zero Pressure Gradient. NACA TN-3178, 1955.

15. Debieve, J.E.; and Lachame, J.P.: A Shock Wave/Free Turbulence Interaction. IUTAM Symposium Palaiseau/France 1985, Turbulent Shear-Layer/ Shock-Wave Interactions, J. Delery, ed., Springer-Verlag, 1985, pp. 394-402.

16. Debieve, J.E.; Gouin, H.; and Gaviglio, J.: Momentum and Temperature Fluxes in a Shock-Wave Turbulence Interaction. Proceedings of ICHMT/IUTAM Symposium on the Structure of Turbulence and Heat and Mass Transfer, Hemisphere Publishing Co., Washington, DC, 1980, pp. 133-136.

17. Ha Minh, H.; and Vandromme, D.D.: Modeling of Compressible Turbulent Flows: Present Possibilities and Perspectives. IUTAM Symposium Palaiseau/ France, Turbulent Shear-Layer/Shock-Wave Interactions, J. Delery, ed., Springer-Verlag, 1985, pp. 13-26.